Nanoscale Advances

ROYAL SOCIETY OF CHEMISTRY

PAPER

View Article Online
View Journal | View Issue

Cite this: *Nanoscale Adv.*, 2021, **3**, 4447

Uniform $MnCo_2O_{4.5}$ porous nanowires and quasi-cubes for hybrid supercapacitors with excellent electrochemical performances†

Xuming Du, Jiale Sun, Runze Wu, Enhui Bao, Chunju Xu * and Huiyu Chen *

In this work, uniform $MnCo_2O_{4.5}$ nanowires (NWs) on stainless steel foil (SSF) were prepared through a facile, cost-efficient, and eco-friendly hydrothermal method at 120 °C with a post-calcination process in air. The microstructure of $MnCo_2O_{4.5}$ samples could be tuned at different hydrothermal temperatures and quasi-cubes (QCs) were obtained in high yield at 150 °C. The $MnCo_2O_{4.5}$ NW powder peeled off from the SSF delivered an outstanding capacity of 248.62 C g^{-1} at 1 A g^{-1} with a capacity preservation of 179.43 C g^{-1} at 8 A g^{-1}, while the QCs exhibited 177.19 and 111.73 C g^{-1}, respectively. To assess the possibility of its actual applications, a hybrid supercapacitor (HSC) device has been assembled by utilizing these $MnCo_2O_{4.5}$ NWs (QCs) and activated carbon (AC) as the cathode and anode, respectively. The $MnCo_2O_{4.5}$ NWs//AC HSC delivered a maximum capacity up to 116.95 C g^{-1} and extraordinary cycling durability with only 3.56% capacity loss over 5000 cycles. Besides, the $MnCo_2O_{4.5}$ NWs//AC HSC achieved a maximum energy density of 25.41 W h kg^{-1} at a power density of 782.08 W kg^{-1}, and for the QC-based HSC, it showed a lower energy density of 20.54 W h kg^{-1} at 843.34 W kg^{-1}. These remarkable electrochemical properties demonstrate that the porous $MnCo_2O_{4.5}$ NWs and QCs may serve as promising cathodes for advanced hybrid supercapacitors with superior performance, and the present synthetic methodology may be applied to the preparation of other cobalt-based binary metal oxides with excellent electrochemical properties.

Received 14th April 2021
Accepted 2nd June 2021

DOI: 10.1039/d1na00271f

rsc.li/nanoscale-advances

1. Introduction

As efficient energy conversion and storage devices, supercapacitors have triggered remarkably increasing attention in the past years owing to their relatively high power density, better cycling durability, faster charging–discharging capability and good rate performance in comparison with conventional rechargeable batteries and capacitors.[1–3] However, the lower energy density of supercapacitors than that of batteries limits their extensive practical application.[4] As a consequence, an urgent concern is to overcome the challenge in the promotion of charge storage capability of supercapacitors without sacrificing the connaturally excellent power density and long cycling life.[5] Generally, energy density is directly determined by the capacitive performance of the cathode and anode in supercapacitors. Therefore, an efficient method to overcome the obstacle of low energy density is to develop electrode materials with porous architectures which can provide large specific surface area and numerous reactive sites.[6,7] Based on the comprehensive knowledge of different energy storage mechanisms, the electrode materials of supercapacitors are usually divided into three sorts such as pseudo-capacitive electrode materials, electric double layer capacitive (EDLC) type materials, and battery-like electrode materials.[8,9]

The energy storage of EDLC electrode materials was achieved through the physical electrostatic charge accumulations in the vicinity of interfaces between the electrode and electrolyte, and no charge transfer during the charging–discharging cycles.[10] Carbonaceous materials are among the typical EDLC electrode materials, and they are extensively studied because of their naturally large specific surface area and they exhibit almost no volume change over long-term cycling processes.[11,12] However, the relatively low specific capacitance may limit the practical application of EDLC electrode materials in some fields where high energy density is required. In pseudo-capacitive electrode materials, the energy storage mechanism is dominated by rapidly reversible faradaic reactions of electrode materials with electrolyte.[13] Metal oxides such as ruthenium dioxide (RuO_2) and manganese dioxide (MnO_2) are widely known to display typical pseudo-capacitive behavior.[14] Moreover, the charge storage of battery-type electrode materials is mainly contributed by the faradaic process which is controlled by ion diffusion kinetics. The main difference is that pseudo-capacitive materials are characterized by EDLC-like electrochemical responses such as distorted rectangle cyclic voltammetry (CV) curves and

School of Materials Science and Engineering, North University of China, Taiyuan, 030051, China. E-mail: chunju@nuc.edu.cn; hychen@nuc.edu.cn

† Electronic supplementary information (ESI) available. See DOI: 10.1039/d1na00271f

triangular galvanostatic charge–discharge (GCD) curves, whereas battery-type materials exhibit both a CV curve with obvious redox peaks and a nonlinear GCD curve with an overt plateau region.[15]

According to the characteristics of electrode materials, supercapacitors are categorized as symmetric supercapacitors (SSCs) and asymmetric supercapacitors (ASCs). The SSCs, such as AC//AC devices, are mainly assembled using the same materials in the cathode and anode through weight matching over charge conservation. However, the low voltage window and rapid attenuation of capacitance along with current density increase limit their widespread applications. In contrast, the ASCs can exhibit wider operating voltage windows and further lead to enhanced capacity/energy density because of the combined contributions from different electrode materials. Particularly, ASCs assembled with battery-type materials as the cathode and carbon-based materials as the anode are called hybrid supercapacitors (HSCs), and the HSCs are expected to show improved energy storage capability.[16]

The electrochemical performance of electrodes plays a significant role in charge storage capability of HSCs. Thus, the key to improving charge storage behavior of HSCs is the controllable fabrication of hierarchical porous active materials with high specific capacity. To date, cobalt-based binary transition metal oxides (BTMOs) with spinel structures, such as $MgCo_2O_4$,[17] $NiCo_2O_4$,[18] $ZnCo_2O_4$,[19,20] $CuCo_2O_4$,[15,21] and $MnCo_2O_{4.5}$,[22] have drawn considerable interest as supercapacitor electrode materials because of their rich valence states, synergistic effects between mixed metal cations, and enhanced capacity features. Among these BTMOs, $MnCo_2O_4$ and $MnCo_2O_{4.5}$ are the most promising battery-grade electrode materials, since the high theoretical specific capacities are mainly ascribed to the multiple valence states of Mn and Co as well as their synergistic influence. But the relatively low conductivity restricts their further wide application to a certain extent. Although significant research efforts have been made with regard to $MnCo_2O_{4.5}$, it is still difficult to achieve its high theoretical specific capacity or extensive operating potential window.[23] Up to now, various microstructures of $MnCo_2O_{4.5}$ have been reported. For instance, urchin-like $MnCo_2O_{4.5}$ with diameter ranging from 4–6 μm was synthesized through a hydrothermal approach and it showed only a capacity of 64.6 C g^{-1} (129.2 F g^{-1}).[24] Liao and coworkers prepared spindle-like $MnCo_2O_{4.5}$ microstructures *via* a solvothermal approach, and the specific capacity of the $MnCo_2O_{4.5}$ microspindles (MSs) was calculated to be 147.49 C g^{-1} (343 F g^{-1}).[25] Cage-like $MnCo_2O_{4.5}$ NPs were prepared through a soft-template assisted method with a calcination process at 600 °C. These irregular $MnCo_2O_{4.5}$ NPs exhibited a poor energy storage capability with 119.2 C g^{-1} (149 F g^{-1}, 0–0.8 V) at 0.2 A g^{-1}, but lost 41.7% of the initial capacity as the current density was enhanced 20 times.[26] Kuang and coworkers reported the growth of $MnCo_2O_{4.5}$ nanoneedle arrays on nickel foam *via* a hydrothermal route, and a high capacity up to 517.9 C g^{-1} could be obtained from these $MnCo_2O_{4.5}$ mesoporous nanoneedle structures.[27] These efforts not only demonstrate that the efficient way to improve energy storage capability and structural stability is controllable preparation of $MnCo_2O_{4.5}$ mesoporous architectures, but also supply an approach to achieve controlled synthesis of $MnCo_2O_{4.5}$ with an appropriate structure providing more redox active sites. Although growing the active material on a substrate can easily control its morphology, the substrate may influence the final capacity to a certain extent. The specific capacities of some $MnCo_2O_{4.5}$-based electrode materials are listed in Table 1.

In this work, we hydrothermally synthesized $MnCo_2O_{4.5}$ with different microstructures on a stainless steel foil (SSF) substrate by changing the hydrothermal reaction temperature. The SSF-supported $MnCo_2O_{4.5}$ has some negative effects when serving as a binder-free electrode material for supercapacitors. It usually possesses large resistance, and the shape exhibits a rigid plate without a three-dimensional porous structure, which may weaken the electron transport and ion diffusion. Particularly, the composition of stainless steel foil from different producers varies, and the accurate composition is difficult to control. In strongly alkaline media, corrosion is probably generated in stainless steel foil more or less, leading to a relatively poor performance of energy storage. Considering the above, the $MnCo_2O_{4.5}$ samples were peeled off from the SSF substrate and the related powder samples were obtained. Grass-like $MnCo_2O_{4.5}$ nanowires (NWs) showed a capacity as high as 248.62 C g^{-1} at 1 A g^{-1}. Meanwhile, 72.17% of the original capacity was preserved as the current density was boosted from 1 to 8 A g^{-1}, indicating an outstanding rate performance. An HSC device with a high operating voltage of 1.75 V in a strongly alkaline electrolyte was assembled using $MnCo_2O_{4.5}$ NWs as the cathode and AC as the anode, respectively. The $MnCo_2O_{4.5}$ NWs//AC HSC displayed both a high energy density of 25.41 W h kg^{-1} at a power density of 782.08 W kg^{-1} and a superior cycling stability with 96.44% capacity retention over 5000 cycles at 4 A g^{-1}.

2. Experimental section

2.1 Synthesis of $MnCo_2O_{4.5}$ on SSF

Chemical reagents of analytical grade were used directly as received, and no additional purification was employed. Before preparing $MnCo_2O_{4.5}$ samples, stainless-steel foil (SSF, 1 cm × 5 cm) was ultrasonically cleaned in diluted hydrochloric acid solution to wipe off surface pollutants, and then washed with anhydrous ethanol and de-ionized (DI) water in sequence. In a typical hydrothermal procedure, 1 mmol of manganese chloride tetrahydrate ($MnCl_2 \cdot 4H_2O$) and 2 mmol of cobalt dichloride hexahydrate ($CoCl_2 \cdot 6H_2O$) powders were placed in a beaker, which contained 40 mL DI water. After all the powders were completely dissolved with magnetic stirring, NH_4F (5 mmol) and urea (5 mmol) were added. With continuous stirring, a pink homogeneous solution was eventually obtained. Later on, the mixed solution and SSF were sealed into a 50 mL autoclave. After a hydrothermal reaction for 6 h at 120 °C, the autoclave was cooled down naturally. The SSF covered with the precursor was rinsed several times using water and anhydrous ethanol, respectively. The dried SSF-supported precursors were placed in a furnace and annealed at 400 °C for 3 h in air. The rate for temperature increase was set to be 5 °C per minute. As the

Table 1 The specific capacity of $MnCo_2O_{4.5}$-based electrode materials

Morphology	Specific surface area ($m^2\ g^{-1}$)	Pore size (nm)	Specific capacity	Ref.
$MnCo_2O_{4.5}$ microspindles	83.3	8.5	147.49 C g^{-1} at 0.5 A g^{-1} (343 F g^{-1}, 0–0.43 V)	25
Urchin-like $MnCo_2O_{4.5}$	22.4	—	59.4 C g^{-1} at 1 A g^{-1} (118.8 F g^{-1}, 0–0.5 V)	24
Pod-like $MnCo_2O_{4.5}$	73.7	12.3	138.03 C g^{-1} at 1 A g^{-1} (321 F g^{-1}, 0–0.43 V)	22
$MnCo_2O_{4.5}$ nanoneedles	—	6.2	517.9 C g^{-1} at 3.6 A g^{-1}	27
Particle-like $MnCo_2O_{4.5}$	97.8	—	105.6 C g^{-1} at 1 A g^{-1} (132 F g^{-1}, 0–0.8 V)	26
$Co_3O_4/MnCo_2O_{4.5}$ core–shell polyhedra	—	—	286.2 C g^{-1} at 1 A g^{-1} (636 F g^{-1}, 0–0.45 V)	36
$MnCo_2O_{4.5}$@GQDs nanoneedles	—	—	812.5 C g^{-1} at 1 A g^{-1} (1625 F g^{-1}, 0–0.5 V)	31
$MnCo_2O_{4.5}$ NWs@δ-MnO_2 nanosheets	42.3	—	357.5 C g^{-1} at 0.5 A g^{-1} (357.5 F g^{-1}, −0.2–0.8 V)	40
Grass-like $MnCo_2O_{4.5}$ NWs	47.03	13.27	248.62 C g^{-1} at 1 A g^{-1}	This work
$MnCo_2O_{4.5}$ QCs	62.64	7.3	177.19 C g^{-1} at 1 A g^{-1}	This work

annealing process was completed, the SSF-supported precursors were converted into black $MnCo_2O_{4.5}$ samples. To find out the morphology difference due to the temperature effect, a series of $MnCo_2O_{4.5}$ microstructures were prepared using the same hydrothermal method but at various hydrothermal reaction temperatures of 100, 130, 140 and 150 °C.

2.2 Material characterization

The detailed structural characterization of the electrode materials is provided in the ESI (S1).†

2.3 Electrochemical measurements

2.3.1 Electrochemical measurements in a three-electrode system. The fabrication of the working electrode and the detailed electrochemical tests in a three-electrode configuration are provided in the ESI (S2).† The specific capacity (C_s, C g^{-1}) of $MnCo_2O_{4.5}$ on the working electrode is obtained according to eqn (1).

$$C_s = \frac{I \times \Delta t}{m} \quad (1)$$

In which I (A) corresponds to the discharging current, Δt (s) denotes the discharging time, and m (g) stands for the mass of $MnCo_2O_{4.5}$.

2.3.2 Electrochemical tests of a HSC in a two-electrode system. A HSC was assembled to further evaluate the electrochemical performance of the $MnCo_2O_{4.5}$ electrode material. The nickel foam loaded with porous $MnCo_2O_{4.5}$ NWs and activated carbon (AC) served as the cathode and anode, respectively, and the device was denoted as $MnCo_2O_{4.5}$ NWs//AC HSC. To obtain the best electrochemical properties, the weight of active materials loaded on the cathode and anode is calculated using eqn (2).[28]

$$\frac{m_+}{m_-} = \frac{C_s^- \times \Delta V^-}{Q_s^+} \quad (2)$$

In which m_+ and m_- mean the weights of active materials loaded on cathode and anode electrodes, respectively. C_s^- represents the specific capacitance (F g^{-1}) of the anode electrode, ΔV^- corresponds to the potential of the charge–discharge curve, and Q_s^+ means the capacity of the cathode electrode. The specific capacity of the HSC (C_{HSC}) and its related energy density (E, W h kg^{-1})/power density (P, W kg^{-1}) are obtained on the basis of eqn (3)–(5), respectively.[15,29] The units of specific capacity are C g^{-1} herein.

$$C_{HSC} = \frac{I\Delta t}{M} \quad (3)$$

$$E = \frac{\int_{t_1}^{t_2} IV_{(t)}\mathrm{d}t}{3.6M} \quad (4)$$

$$P = \frac{3600E}{\Delta t} \quad (5)$$

In which I (A) is the constant current used in the HSC, Δt (s) corresponds to the discharge time, M (g) means the gross weight of $MnCo_2O_{4.5}$ NWs and AC on the positive and negative electrodes, and t_1 and t_2 stand for the preliminary time after IR drop and ending time of the discharging process, respectively.

3. Results and discussion

The crystalline structure of the as-synthesized $MnCo_2O_{4.5}$ was analyzed using XRD. As displayed in Fig. 1a, diffraction peaks centered at 2θ values of 19.0°, 31.3°, 36.8°, 38.5°, 44.8°, 55.8°, 59.5°, and 65.3° could be observed, which well correspond to the (111), (220), (311), (222), (400), (422), (511), and (440) planes of $MnCo_2O_{4.5}$ with a spinel structure (JCPDS no. 32-0297), consistent with those in the reported literature.[25,30] No other characteristic peaks appeared in the XRD pattern, indicating that high purity of the $MnCo_2O_{4.5}$ sample was obtained after a thermal annealing in air. The sharp peaks in the XRD pattern implied that the $MnCo_2O_{4.5}$ microstructures calcined at 400 °C for 3 h were well-crystallized. In the synthetic process, urea serves as a precipitator for the fabrication of the precursor because it can provide an alkaline medium. The urea molecules undergo hydrolysis at high temperature, and the final product of the hydrolysis reaction contains CO_3^{2-}, NH_4^+, and OH^- ions, so a weakly alkaline medium can be formed. The manganese and cobalt cations in the solution may react with the anions to form a precursor, and then the precursor will be converted into related metal oxides during annealing treatment. The surface

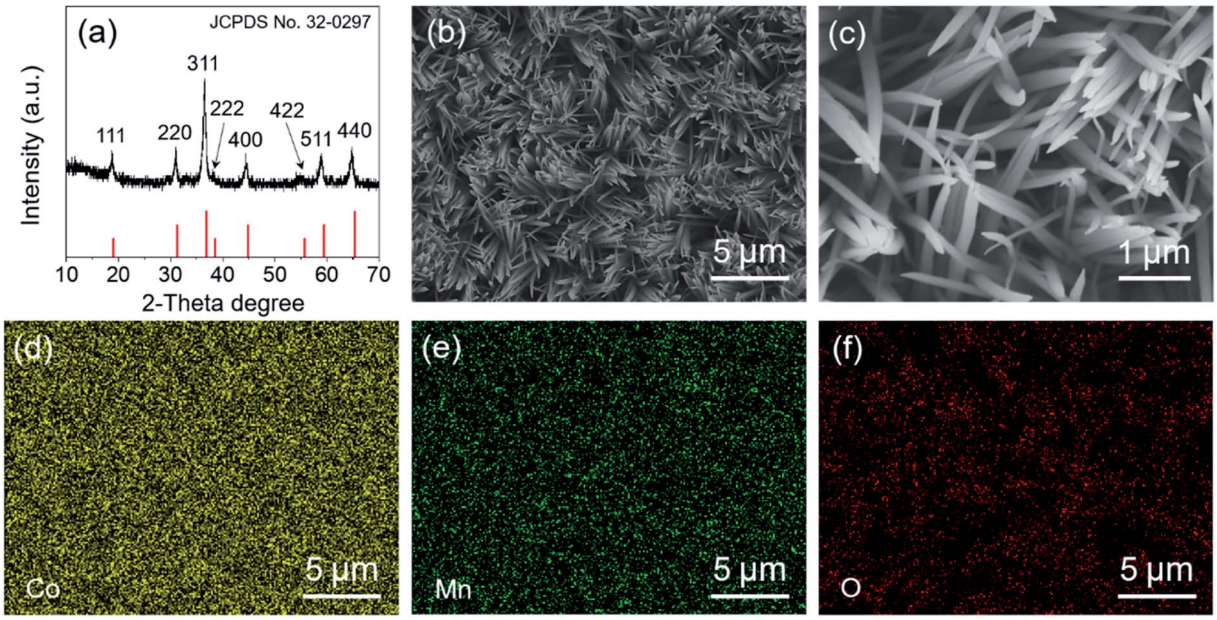

Fig. 1 Crystal phase and morphological investigations of the SSF-supported $MnCo_2O_{4.5}$ NWs prepared at 120 °C for 6 h followed by an annealing treatment at 400 °C for 3 h: (a) XRD pattern, (b and c) SEM images at different magnifications, and the related EDS elemental mapping images taken from the position of (b) for (d) Co, (e) Mn, and (f) O, respectively.

morphology and structures of $MnCo_2O_{4.5}$ were investigated by FESEM. As presented in Fig. 1b and c, grass-like $MnCo_2O_{4.5}$ NW arrays could be observed in the SEM images. It was clearly seen that the SSF substrate was nearly completely covered by luxuriant grass-like NWs with a diameter of approximately 50–200 nm in the middle positions. Fig. 1d–f display the corresponding elemental distributions of Co, Mn and O. Obviously, the three elements were uniformly distributed in these $MnCo_2O_{4.5}$ NWs.

TEM and high-resolution TEM (HRTEM) characterization studies were performed to acquire insights into the morphology and microstructure of $MnCo_2O_{4.5}$ NWs. Fig. 2a shows the TEM image of a $MnCo_2O_{4.5}$ NW with a diameter of approximately 100 nm. Meanwhile, it could be seen that the individual NW was assembled by numerous nanoparticles (NPs). Plenty of pores between the adjacent NPs were also observed, and they could facilitate the diffusion of electrolyte ions. The selected area electron diffraction (SAED) pattern (Fig. 2b) showed that the ED rings consisted of dispersive spots, indicating the polycrystalline characteristic of these $MnCo_2O_{4.5}$ NWs. The high-resolution TEM image shown in Fig. 2c exhibits distinct lattice fringes with different orientations. The close-up high-resolution TEM image (Fig. 2d) for the selected position in Fig. 2c shows an interplanar spacing of 0.234 nm, which is well ascribed to the (222) crystal planes of cubic spinel $MnCo_2O_{4.5}$.

The elemental valence states of $MnCo_2O_{4.5}$ NWs were further identified through X-ray photoelectron spectroscopy (XPS) analysis, and Fig. 3 presents the corresponding XPS spectra. The binding energies of Co 2p, Mn 2p, and O 1s were revised by referring them to the 284.6 eV of C 1s. The full survey XPS spectrum (Fig. 3a) confirmed the coexistence of Co, Mn, and O. As depicted in the Co 2p XPS spectrum (Fig. 3b), the characteristic peaks of Co $2p_{1/2}$ and Co $2p_{3/2}$ were centered at 795.3 and 780.1 eV (energy gap: 15.2 eV), accompanied by two shake-up satellite peaks at 786.4 and 803.2 eV. It indicated the coexistence of cobalt species including Co^{2+} and Co^{3+} in the $MnCo_2O_{4.5}$ NWs.[25,30] By refined fitting, the two major peaks in the Co 2p spectrum could be divided into four sub-peaks using the Gaussian fitting method, and the peaks at 781.7 and 797.1 eV were assigned to Co^{2+}, whereas the peaks at 780.0 and 795.2 eV were ascribed to Co^{3+}. Similarly, two closely adjacent peaks at 641.9 and 653.5 eV were observed in the fitted XPS spectrum of Mn 2p (Fig. 3c), which correspond to Mn $2p_{3/2}$ and Mn $2p_{1/2}$. The fitted peaks at the positions of 641.6 and 653.2 eV were ascribed to Mn^{2+}, while the other two sub-peaks at 643.5 and 655.2 eV were attributed to Mn^{3+}.[31] Furthermore, the O 1s spectrum in Fig. 3d exhibits three fitted peaks at 529.9 (O1), 531.2 (O2), and 532.6 eV (O3), which determined the oxygen in the metal–oxygen bond (Mn/Co–O), the oxygen in hydroxyl groups, and the oxygen in water molecules physically and chemically absorbed on the surface of $MnCo_2O_{4.5}$ NWs, respectively.[32] On the whole, the XPS data proved that Co^{2+}, Co^{3+}, Mn^{2+}, and Mn^{3+} appeared simultaneously in $MnCo_2O_{4.5}$, and it also directly confirmed the successful preparation of $MnCo_2O_{4.5}$ NWs in a highly pure phase through an easy and cost-effective hydrothermal route with post-annealing treatment.

There are some parameters including concentration of chlorates, hydrothermal temperature, and the dosage of NH_4F and urea which may play significant roles in the growth of $MnCo_2O_{4.5}$ microstructures with diverse shapes. In this work, control experiments were conducted at different hydrothermal temperatures. As shown in Fig. 4, the SEM images displayed the morphological changes of different $MnCo_2O_{4.5}$

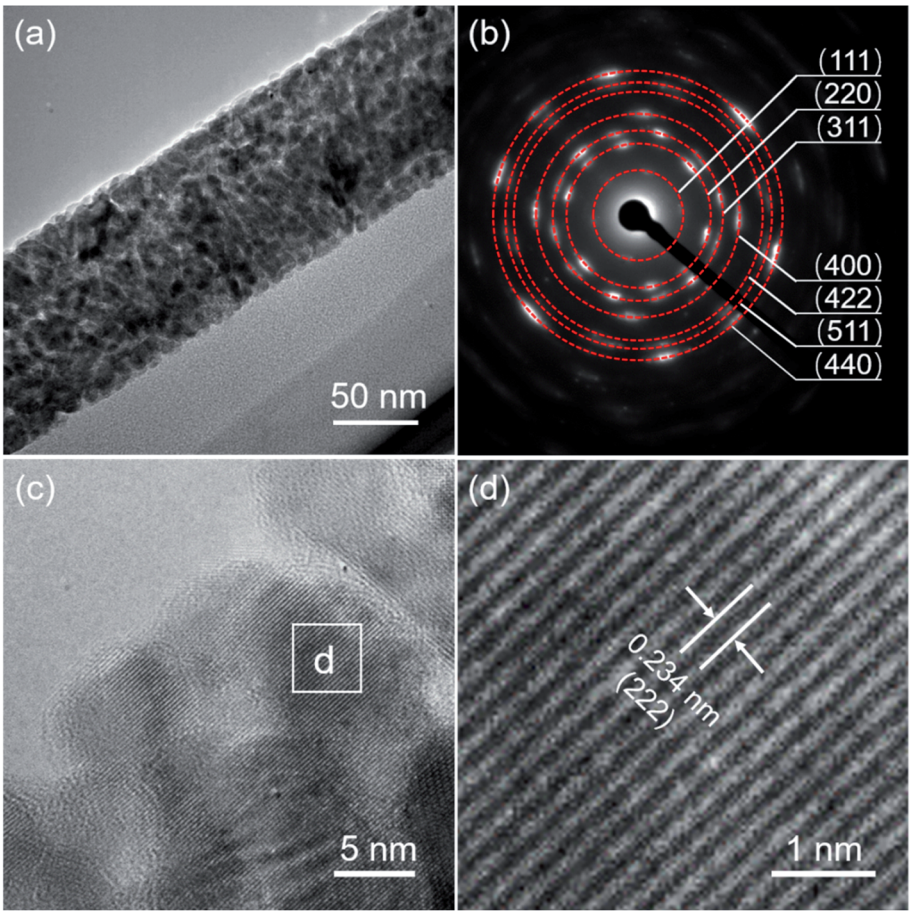

Fig. 2 TEM characterization of a $MnCo_2O_{4.5}$ NW removed from the SSF substrate: (a) TEM image, (b) related SAED pattern, (c) high-resolution TEM image, and (d) magnified high-resolution TEM image from the selected position in (c).

microstructures prepared at various hydrothermal temperatures. Fig. 4a shows that the clusters of grass-like $MnCo_2O_{4.5}$ microstructures were homogeneously distributed on the SSF substrate when the hydrothermal temperature was as low as 100 °C, but the yield was not high to some extent. After 6 h of reaction at 100 °C, the solution in the autoclave still remained pink, suggesting that the reaction was not totally completed. A large amount of NWs were obtained at 120 °C (Fig. 1b). When the temperature was increased to 130 °C, a few $MnCo_2O_{4.5}$ quasi-cube (QC) microstructures emerged in the NWs (Fig. 4b). The QCs were composed of a lot of microflakes, and some cusps of NWs on the surface of layered QCs were also observed. $MnCo_2O_{4.5}$ QCs gradually dominated in the products with the increase of hydrothermal temperature (Fig. 4c). Finally, the grass-like $MnCo_2O_{4.5}$ NWs completely disappeared as the temperature was further increased to 150 °C, and these QCs possessed three edges perpendicular to each other (Fig. 4d). As the temperature was increased, the reactions proceeded more rapidly, leading to the formation of less anisotropic QCs. To synthesize micro-/nano-structures with a more anisotropic shape, the reaction should proceed slowly enough in order that the initial nucleation stage can be isolated from the subsequent crystal growth stage. Anisotropic $MnCo_2O_{4.5}$ NWs as the sole final product could be obtained at temperatures below 120 °C.

The porosity and pore size distribution as well as the surface area for $MnCo_2O_{4.5}$ NWs at 120 °C and $MnCo_2O_{4.5}$ QCs at 150 °C were examined utilizing N_2 adsorption–desorption isotherms, and the isotherms in Fig. 5a and c were categorized as type-IV with an obvious type-H3 loop, indicating the typical mesoporous nature of $MnCo_2O_{4.5}$ samples. The BET specific surface area of $MnCo_2O_{4.5}$ NWs was evaluated to be 47.03 $m^2 g^{-1}$, and the corresponding pore size distribution was found to be centered at 8.7 nm with an average pore size of 13.27 nm. The existence of mesopores confirmed the observation from the TEM image. In contrast, the $MnCo_2O_{4.5}$ QCs possessed a BET specific surface area of 62.64 $m^2 g^{-1}$, a smaller BJH average pore size of 7.38 nm and a main pore size of approximately 7.3 nm. Obviously, the specific surface areas increased with the shape of $MnCo_2O_{4.5}$ changing from NWs to QCs. Similarly, both the average pore size and main pore size distribution of $MnCo_2O_{4.5}$ QCs were smaller than those of $MnCo_2O_{4.5}$ NWs. The QCs exhibit a very large size of about 10–15 μm (Fig. 4d), and smaller pores may be generated in the inside during the calcination process. In

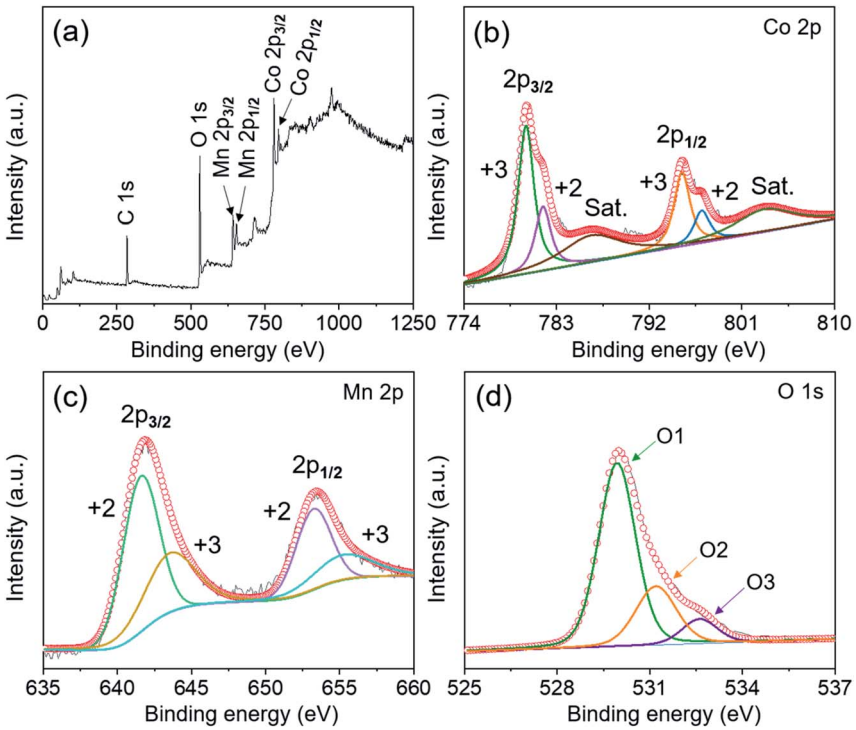

Fig. 3 (a) XPS survey spectrum of the $MnCo_2O_{4.5}$ NW powder separated from stainless steel foil and high resolution XPS spectra for (b) Co 2p, (c) Mn 2p, and (d) O1s, respectively.

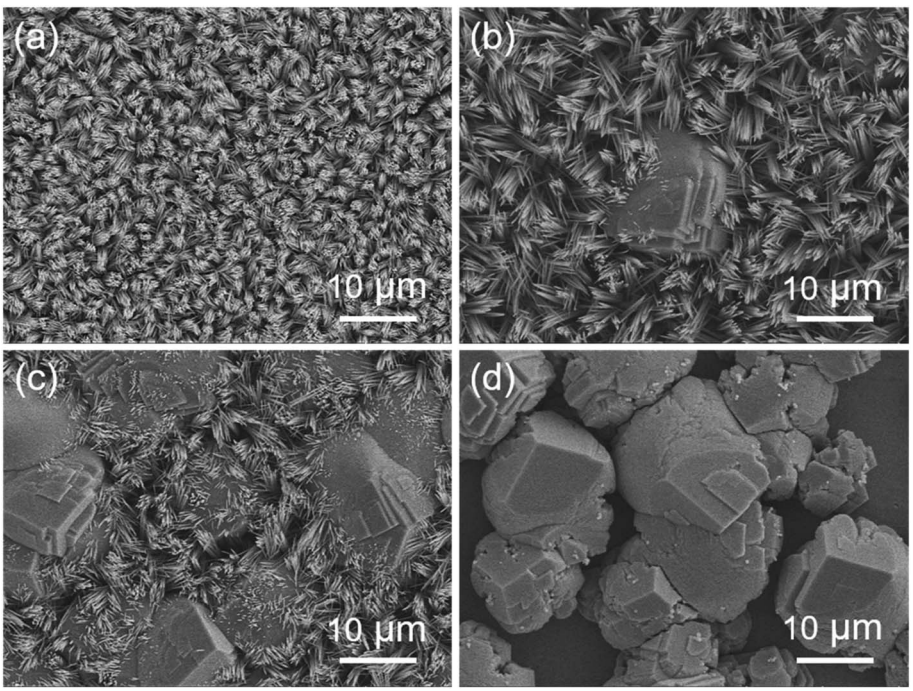

Fig. 4 SEM images of $MnCo_2O_{4.5}$ samples prepared at different hydrothermal temperatures of (a) 100, (b) 130, (c) 140, and (d) 150 °C, respectively. All samples were processed with an annealing treatment at 400 °C for 3 h.

comparison, the NWs are relatively thin in diameter, and they can experience sufficient calcinations, resulting in larger pores as well as smaller surface area.

The electrochemical storage performances of $MnCo_2O_{4.5}$ NWs and QCs were investigated in a three-electrode system through CV, GCD and EIS tests. The typical three-electrode

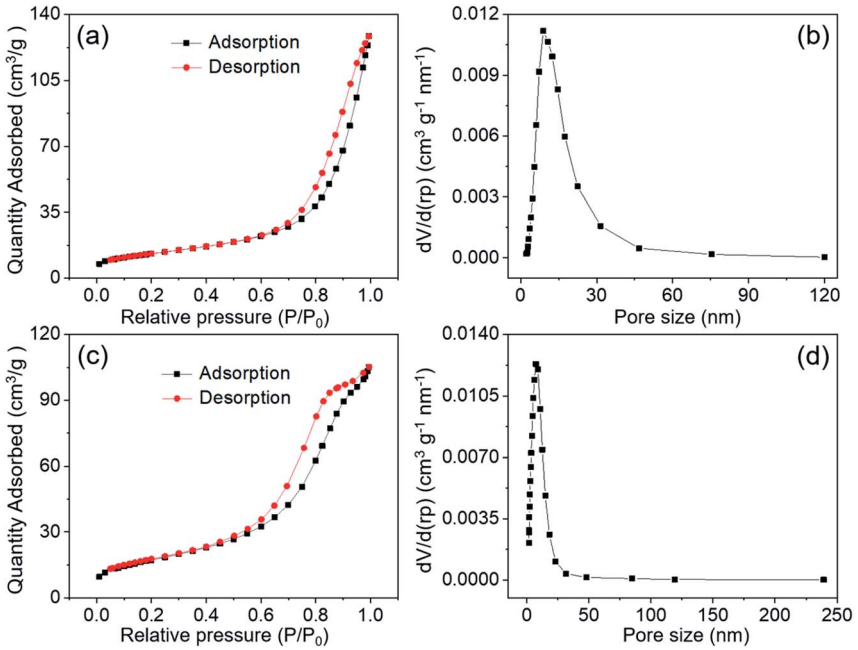

Fig. 5 (a) Nitrogen adsorption–desorption isotherms and (b) the related BJH pore size of $MnCo_2O_{4.5}$ NWs obtained at 120 °C, and (c) nitrogen adsorption–desorption isotherms and (d) the related BJH pore size of $MnCo_2O_{4.5}$ QCs obtained at 150 °C.

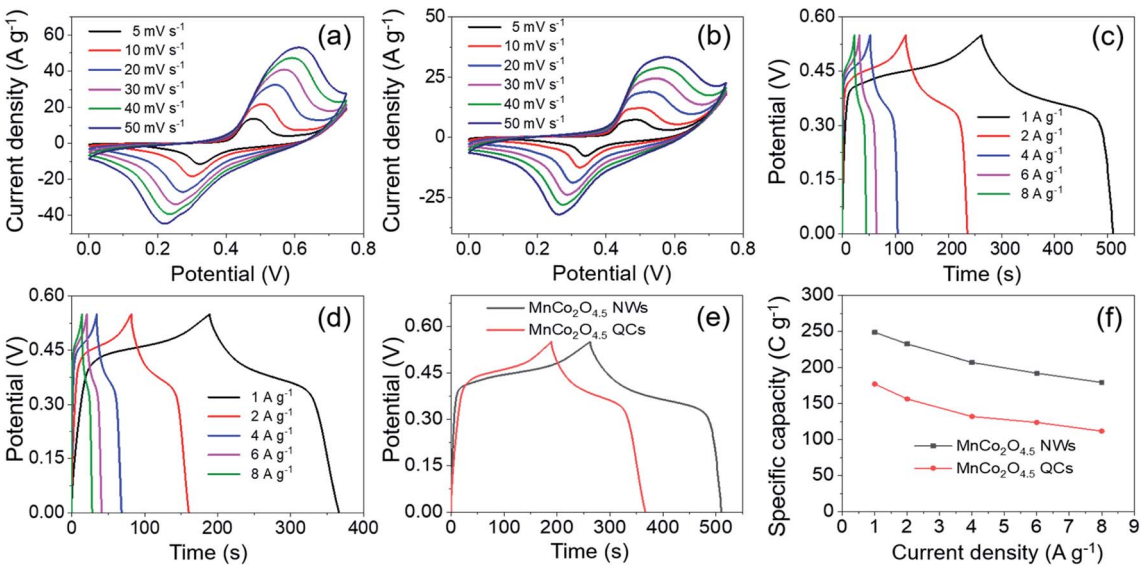

Fig. 6 Electrochemical tests of $MnCo_2O_{4.5}$ NWs and $MnCo_2O_{4.5}$ QCs in a three-electrode system using 2 M KOH electrolyte: CV curves of (a) $MnCo_2O_{4.5}$ NWs and (b) $MnCo_2O_{4.5}$ QCs at different scan rates of 5–50 mV s^{-1}, GCD curves of (c) $MnCo_2O_{4.5}$ NWs and (d) $MnCo_2O_{4.5}$ QCs at different current densities of 1–8 A g^{-1}, (e) GCD curves of $MnCo_2O_{4.5}$ NWs and $MnCo_2O_{4.5}$ QCs at 1 A g^{-1}, and (f) the rate performances of $MnCo_2O_{4.5}$ NWs and $MnCo_2O_{4.5}$ QCs at various current densities.

configuration contained the Ni foam loaded with $MnCo_2O_{4.5}$ powder scraped from the SSF substrate, Hg/HgO, and Pt-foil as the working, reference, and counter electrodes, respectively. Freshly prepared 2 M KOH solution served as the electrolyte. As exhibited in Fig. 6a and b, the CV curves of $MnCo_2O_{4.5}$ NWs and $MnCo_2O_{4.5}$ QCs were obtained at different scan rates (5–50 mV s^{-1}) under potential windows between 0 and 0.75 V. All CV curves exhibited a similar shape with a couple of well-defined cathodic and anodic peaks, indicating that $MnCo_2O_{4.5}$ NWs and QCs delivered an obvious battery-type electrochemical response rather than pseudo-capacitive (quasi-rectangular CV curves) or EDLC-type (rectangular CV curves) electrochemical behavior. The plausible redox reactions can be described as follows:[31]

$$MnCo_2O_{4.5} + H_2O + OH^- \leftrightarrow MnOOH + CoOOH + e^- \quad (6)$$

$$MnOOH + OH^- \leftrightarrow MnO_2 + H_2O + e^- \quad (7)$$

Meanwhile, the cathodic/anodic peaks shifted to more negative/positive directions with an increase of scan rate, respectively, which could be mainly ascribed to the polarization at high sweep rate. These observations suggested that fast and reversible faradaic reactions proceeded at the electrode–electrolyte interface, which well matched with that reported in previous literature.[33] Furthermore, the CV curves of $MnCo_2O_{4.5}$ NWs exhibited higher cathodic and anodic current densities as well as an apparently larger integrated area compared with those of $MnCo_2O_{4.5}$ QCs, indicating that the $MnCo_2O_{4.5}$ NW electrode possessed higher specific capacity than $MnCo_2O_{4.5}$ QCs. Fig. S1† provides the curves of peak current (i_p) *vs.* the square root of scan rate ($v^{1/2}$) for both $MnCo_2O_{4.5}$ NWs and QCs, and the proportional relationship indicated that the charge storage procedure was governed by ion diffusion. In addition, the capacitive contribution can be determined using $^{i}(V) = k_1v + k_2v^{1/2}$. At a fixed potential V, the total current response i can be divided into both the current resulting from capacitive reactions (k_1v) and the current induced by diffusion-controlled reactions ($k_2v^{1/2}$). After determining the k_1 and k_2 constants, the quantitative analysis in Fig. S2a and b† indicated that the capacitive contributions were 85% and 88% of the entire charge storage for $MnCo_2O_{4.5}$ NWs and QCs at 40 mV s^{-1}. With the scan rate increasing from 5 to 50 mV s^{-1}, the capacitive contribution for $MnCo_2O_{4.5}$ NWs increased from 56% to 92% (Fig. S2c†), while for the QCs, the value improved from 59% to 93% accordingly (Fig. S2d†).

GCD measurements were carried out to study the specific capacity and rate performance of the $MnCo_2O_{4.5}$ NWs and QCs, and Fig. 6c and d present the corresponding GCD curves at different current densities in the potential window of 0–0.55 V. The specific capacity of $MnCo_2O_{4.5}$ NWs was calculated from eqn (1) and it delivered the values of 248.62, 232.42, 207.12, 192.24, and 179.43 C g^{-1} at 1, 2, 4, 6, and 8 A g^{-1}, respectively. In comparison, the $MnCo_2O_{4.5}$ QCs exhibited specific capacities of 177.19, 156.35, 132.03, 123.73, and 111.73 C g^{-1} at each current density, respectively. The specific capacity of $MnCo_2O_{4.5}$ NWs was higher than that of $MnCo_2O_{4.5}$ QCs. The remarkably enhanced specific capacity of $MnCo_2O_{4.5}$ NWs could be ascribed to the existence of mesopores in the thin NWs, which generated numerous channels for ion diffusion and electron transport. However, for the $MnCo_2O_{4.5}$ QC electrode material, due to the huge total size of QCs, the diffusion of ions and electrons was hampered in the inside of QCs, and therefore, slower reaction kinetics could occur during the charge–discharge process. Fig. 6e shows the GCD curves of NWs and QCs at 1 A g^{-1}, and obviously the discharge time of NWs was longer than that of QCs, suggesting the higher capacity of NWs. Fig. 6f illustrates the relationship between specific capacity and corresponding current density. It was clear that capacity decreased with current density increasing, which could be explained by two reasons. On the one hand, a large voltage drop always appears at high current density, and it may cause negative influence on the capacity. On the other hand, inadequate contact between

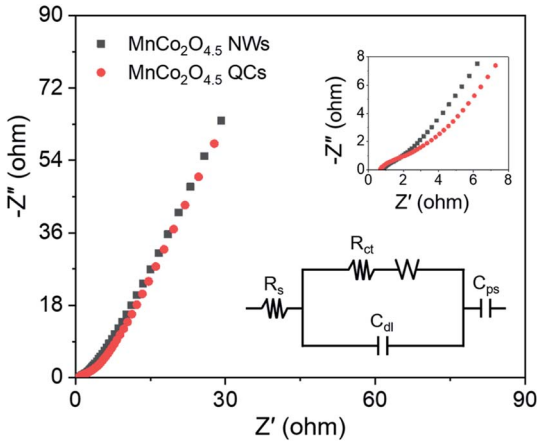

Fig. 7 The Nyquist plots of $MnCo_2O_{4.5}$ NWs and QCs, and the inset shows the enlarged plots in the high-frequency region as well as a fitted equivalent circuit.

$MnCo_2O_{4.5}$ and the electrolyte was also negative for the contribution of capacity because of the short discharging time at high current density.

To further evaluate the internal resistance and reaction kinetics of the $MnCo_2O_{4.5}$ NWs and QCs, EIS tests were carried out at frequencies between 0.01 Hz and 100 kHz under an open circuit potential by applying an AC voltage of 5 mV amplitude. The Nyquist plots of $MnCo_2O_{4.5}$ NWs and QCs at room temperature are shown in Fig. 7, which were fitted with an equivalent circuit. The equivalent circuit comprised an internal resistance R_s (including the intrinsic resistance of $MnCo_2O_{4.5}$, contact resistance between $MnCo_2O_{4.5}$ and Ni foam, and ionic resistance of KOH aqueous electrolyte), an electron transfer resistance R_{ct}, and a Warburg resistance W. The R_s was directly determined from the intercepts of the X-axis, and the values for $MnCo_2O_{4.5}$ NWs and QCs were found to be 0.81 and 0.67 Ω, respectively. With respect to the R_{ct} resistance, the determined values for NWs and QCs were 0.83 and 0.76 Ω. Both the $MnCo_2O_{4.5}$ NWs and QCs in this work exhibited much lower R_s values than the previously reported Mn/Co-oxide-based materials.[26,27,34] In addition, the slope of the straight line at the low frequency region reflected Warburg resistance, which was influenced by the ion diffusion in faradaic reactions between the interface of $MnCo_2O_{4.5}$ electrodes and KOH electrolyte. It indicated the good conductivity of both $MnCo_2O_{4.5}$ NWs and QCs.

In order to investigate the actual application of porous $MnCo_2O_{4.5}$ NWs and QCs, a hybrid supercapacitor ($MnCo_2O_{4.5}$ NWs//AC HSC and $MnCo_2O_{4.5}$ QCs//AC HSC) device was assembled with the NWs (QCs) and AC as the cathode and anode, respectively. As we reported previously, the AC used herein possessed a specific capacitance of 178.5 F g^{-1} (−1.0–0.0 V) at 1 A g^{-1} and splendid rate durability (retained 87% of the original capacitance at 16 A g^{-1}),[2] illustrating that the AC was suitable as the anode material for supercapacitor applications. The optimal weight ratio of m_+/m_- was determined according to eqn (2). To achieve the optimal electrochemical properties of

the HSC, a series of CV tests were conducted at a scan rate of 10 mV s^{-1} with the voltage varying between 0–1.2 and 0–1.8 V to ascertain the voltage window of the $MnCo_2O_{4.5}$ NWs//AC HSC. The CV curves obtained with the voltage window of 0–1.8 V (Fig. S3a†) showed a distinct polarization phenomenon. The GCD curves shown in Fig. S3b† were recorded under various voltage windows from 0–1.2 to 0–1.75 V at 1 A g^{-1}, and all GCD profiles displayed a typical feature of quasi isosceles triangle with an imperceptible IR drop. As a consequence, the appropriate operating voltage window of the $MnCo_2O_{4.5}$ NWs//AC HSC was demonstrated to be 0–1.75 V. Fig. S3c† illustrates the specific capacities under different voltage windows, and the capacity increased from 62.34 C g^{-1} at 0–1.2 V to 116.95 C g^{-1} at 0–1.75 V. Moreover, energy density showed an upward trend from 10.76 to 25.41 W h kg^{-1} accordingly (Fig. S3d†).

CV and GCD measurements of the $MnCo_2O_{4.5}$ NWs//AC HSC were carried out within the voltage window of 0–1.75 V. Fig. 8a shows that all the corresponding CV curves manifested a distorted rectangular shape containing broad redox peaks, and the shape remained unchanged with the increase of scan rate, indicating a characteristic capacitive behavior caused by the assembly of battery-type and EDLC electrodes. Symmetrical GCD curves with a nonlinear nature as shown in Fig. 8c were obtained with a variety of current densities, and the plateau region on these curves verified the existence of faradaic reactions during the charge–discharge process. Meanwhile, the specific capacity of the $MnCo_2O_{4.5}$ NWs//AC HSC was calculated through eqn (3), and the values could reach 116.95, 103.80, 92.96, 87.34 and 82.44 C g^{-1} at 1, 2, 4, 6 and 8 A g^{-1}, respectively. Approximately 70.49% of the initial capacity was retained when the current density was raised from 1 to 8 A g^{-1}, indicating that the $MnCo_2O_{4.5}$ NWs//AC HSC possessed a good rate capability. To make a comparison, the $MnCo_2O_{4.5}$ QCs//AC HSC was also assembled with a fabrication process similar to that of the $MnCo_2O_{4.5}$ NWs//AC HSC, and CV and GCD measurements were performed under the same conditions (Fig. 8b and d). Compared with the $MnCo_2O_{4.5}$ NWs//AC HSC, the $MnCo_2O_{4.5}$ QCs//AC HSC exhibited lower specific capacities of 87.67, 75.93, 65.70, 61.42, and 56.90 C g^{-1} accordingly. Fig. 8e directly provides the GCD curves of the HSCs at 1 A g^{-1}, which clearly exhibited the longer discharging time of the $MnCo_2O_{4.5}$ NWs//AC HSC than that of the $MnCo_2O_{4.5}$ QCs//AC HSC. The rate performances of both NW- and QC-based HSCs are shown in Fig. 8f, respectively.

It is generally known that the cycling property of HSC devices plays a vital role in determining the actual application of electro-active electrode materials. Repeated GCD tests were performed to study the cycling performance of $MnCo_2O_{4.5}$ NWs//AC and $MnCo_2O_{4.5}$ QCs//AC HSCs at 4 A g^{-1}, as presented in Fig. 9. Over 5000 continuous cycles, the $MnCo_2O_{4.5}$ NWs//AC HSC device exhibits a long-term cycling durability with 96.44% retention of its initial capacity. The inset in Fig. 9a displays the last ten cycles, and no obvious changes in the symmetrical curves were observed, demonstrating an excellent cycling durability of the $MnCo_2O_{4.5}$ NWs//AC HSC. In addition, the $MnCo_2O_{4.5}$ QCs//AC HSC maintained a specific capacity from the initial 65.70 to final 64.25 C g^{-1} after 5000 cycles, suggesting 97.79% capacity retention. The coulombic efficiency (η) can be calculated using eqn (8), and both the HSCs achieved almost perfect η values (~100%) during the entire 5000 GCD cycles.

$$\eta = \frac{t_d}{t_c} \times 100\% \quad (8)$$

where t_d and t_c are defined as the discharging and charging time, respectively. Thus, it suggested that the faradaic reactions

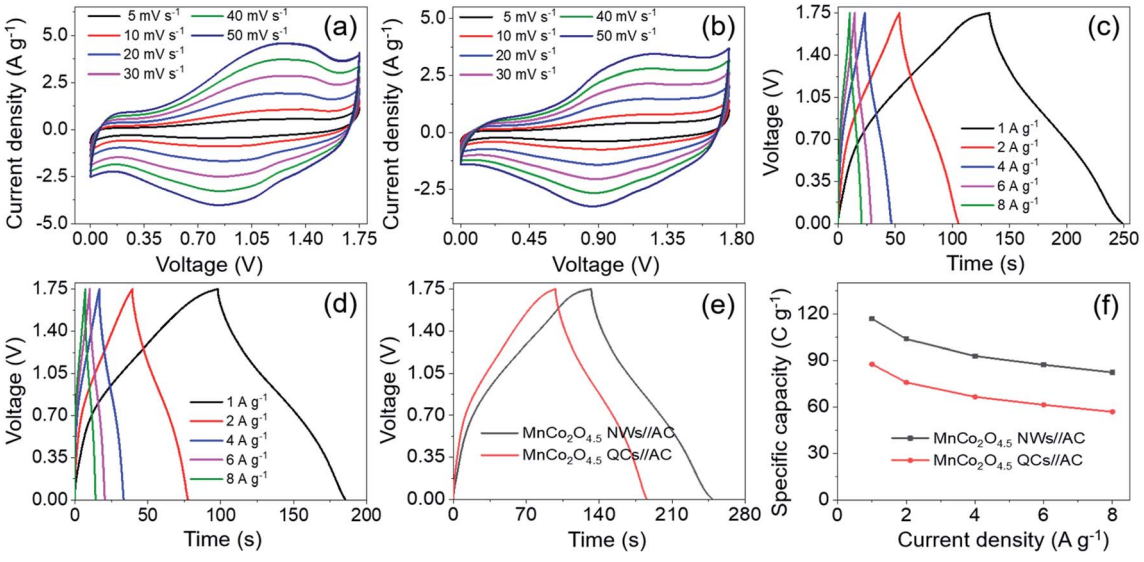

Fig. 8 Electrochemical tests of $MnCo_2O_{4.5}$ NWs//AC and $MnCo_2O_{4.5}$ QCs//AC HSCs in a two-electrode system using 2 M KOH electrolyte: CV curves of (a) $MnCo_2O_{4.5}$ NWs//AC and (b) $MnCo_2O_{4.5}$ QCs//AC HSCs at different scan rates, GCD curves of (c) $MnCo_2O_{4.5}$ NWs//AC and (d) $MnCo_2O_{4.5}$ QCs//AC HSCs at different current densities, (e) GCD curves of $MnCo_2O_{4.5}$ NWs//AC and $MnCo_2O_{4.5}$ QCs//AC HSCs at 1 A g^{-1}, and (f) the rate performances of $MnCo_2O_{4.5}$ NWs//AC and $MnCo_2O_{4.5}$ QCs//AC HSCs.

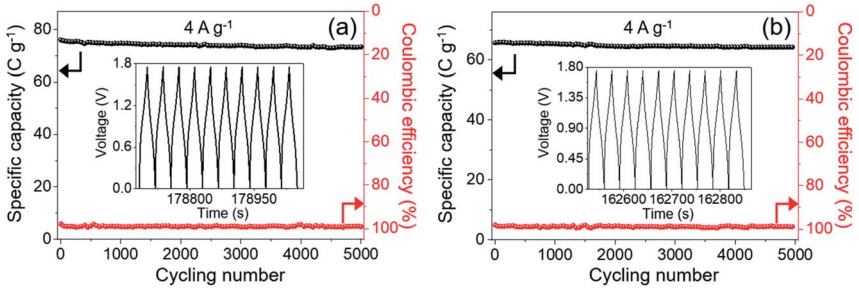

Fig. 9 Cycling tests and coulombic efficiency of (a) $MnCo_2O_{4.5}$ NWs//AC and (b) $MnCo_2O_{4.5}$ QCs//AC HSCs during 5000 cycles at 4 A g^{-1}, and the insets provide the last ten GCD curves.

are almost completely reversible during the operations of HSCs.

The Ragone plots of $MnCo_2O_{4.5}$ NWs//AC and $MnCo_2O_{4.5}$ QCs//AC HSCs are illustrated (Fig. 10) along with a comparison of some Mn/Co-based asymmetrical supercapacitors (ASCs) reported in recent literature. The corresponding energy density and power density were obtained through eqn (4) and (5). The $MnCo_2O_{4.5}$ NWs//AC HSC achieved an energy density of 25.41 W h kg^{-1} at a power density of 782.08 W kg^{-1} and still retained 18.18 W h kg^{-1} even at a higher power density of 6.35 kW kg^{-1}. In contrast, the $MnCo_2O_{4.5}$ QCs//AC HSC exhibited a lower energy density of 20.54 W h kg^{-1} at 843.34 W kg^{-1}. As illustrated in the Ragone plots, the $MnCo_2O_{4.5}$ NWs//AC HSC possessed superior or comparable energy density to the $MnCo_2O_{4.5}$ QCs//AC HSC and some other ASCs assembled with battery-type Mn/Co-based oxides as the cathode, such as $MnCo_2O_4$ nanorods//AC (12.77 W h kg^{-1} at 138.40 W kg^{-1}),[35] $MnCo_2O_{4.5}$ pods//AC (19.65 W h kg^{-1} at 810.64 W kg^{-1}),[22] $Co_3O_4/MnCo_2O_{4.5}$//nanoporous carbon (23 W h kg^{-1} at 796 W kg^{-1}),[36] $Ni_{0.5}Mn_{0.5}Co_2O_4$ nanoflowers//AC (20.2 W h kg^{-1} at 700 W kg^{-1}),[37] and $NiMnCoO_4$//reduced graphene oxide ($NiMnCoO_4$//rGO, 20 W h kg^{-1} at 377 W kg^{-1}).[28] However, the value was still inferior to some of the ASCs such as $MnCo_2O_{4.5}$@graphene quantum dots//reduced graphene oxide ($MnCo_2O_{4.5}$@GQDs//rGO, 44 W h kg^{-1} at 66 W kg^{-1}),[31] $MnCo_2O_4$ nanosheets//AC (33.8 W h kg^{-1} at 318.9 W kg^{-1}),[38] and $MnCo_2O_4$ porous spheres (PSs)//starch-derived carbon foam (SCF) (42.27 W h kg^{-1} at 400 W kg^{-1}).[39] Based on the above electrochemical performances of $MnCo_2O_4$ NWs and the corresponding HSC, the porous $MnCo_2O_4$ NWs herein can provide a promising application as an advanced battery-grade electrode material for high-performance HSC devices.

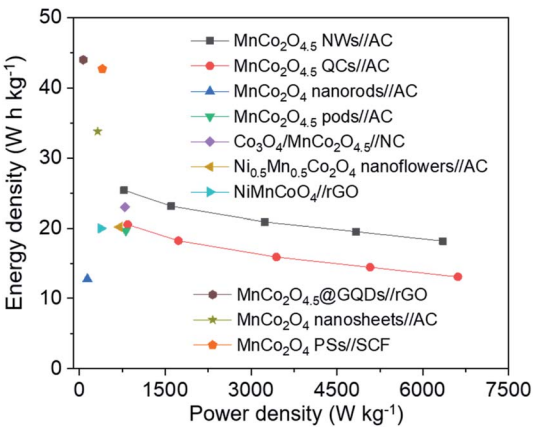

Fig. 10 Ragone plots of the $MnCo_2O_{4.5}$ NWs//AC HSC, $MnCo_2O_{4.5}$ QCs//AC HSC, and some other related ASCs reported previously.

4. Conclusions

In conclusion, porous $MnCo_2O_{4.5}$ NWs and QCs could be prepared with a uniform structure using stainless steel foil as a substrate through a facile, cost-effective, and eco-friendly hydrothermal method along with an extra calcination in air. The shape and structure of $MnCo_2O_{4.5}$ were controlled through hydrothermal reaction temperature. It was demonstrated that the $MnCo_2O_{4.5}$ NW powder possessed better electrochemical performance than QCs. The $MnCo_2O_{4.5}$ NWs achieved a significant specific capacity of 248.62 C g^{-1} at a current density of 1 A g^{-1} and maintained a capacity of 179.43 C g^{-1} at 8 A g^{-1}, while the QCs delivered 177.19 (1 A g^{-1}) and 111.73 C g^{-1} (8 A g^{-1}), respectively. To investigate the practical application of $MnCo_2O_{4.5}$, a HSC device was constructed using $MnCo_2O_{4.5}$ NWs (QCs) and AC as the cathode and anode, respectively. The $MnCo_2O_{4.5}$ NWs//AC HSC device exhibited a specific capacity of 116.95 C g^{-1} at 1 A g^{-1}, a good rate capability with 70.49% capacity retention at 8 A g^{-1}, and an extraordinary cycling durability with only 3.56% capacity decay after 5000 cycles. Furthermore, the HSC achieved an energy density of 25.41 W h kg^{-1} at a power density of 782.08 W kg^{-1}. At a higher power density of 6.35 kW kg^{-1}, such a HSC still delivered an energy density of 18.18 W h kg^{-1}. These remarkable electrochemical results demonstrated an efficient approach to prepare $MnCo_2O_{4.5}$ with a controllable structure and superior electrochemical properties using stainless steel foil as a supporting substrate. The present method can also be used for synthesizing other spinel cobalt-based oxides to serve as battery-type cathode electrode materials for next-generation high-performance hybrid supercapacitors.

Conflicts of interest

There are no conflicts to declare.

Acknowledgements

This work was supported by the Shanxi Scholarship Council of China.

References

1 S. Liu, D. Ni, H. F. Li, K. N. Hui, C. Y. Ouyang and S. C. Jun, Effect of cation substitution on the pseudocapacitive performance of spinel cobaltite MCo_2O_4 (M = Mn, Ni, Cu, and Co), *J. Mater. Chem. A*, 2018, **6**, 10674–10685.

2 Y. Wang, X. Ma, S. Li, J. Sun, Y. Zhang, H. Chen and C. Xu, Facile solvothermal synthesis of novel $MgCo_2O_4$ twinned-hemispheres for high performance asymmetric supercapacitors, *J. Alloys Compd.*, 2020, 818.

3 J. Li, D. Xiong, L. Wang, M. K. S. Hirbod and X. Li, High-performance self-assembly $MnCo_2O_4$ nanosheets for asymmetric supercapacitors, *J. Energy Chem.*, 2019, **37**, 66–72.

4 G. M. Thorat, H. S. Jadhav and J. G. Seo, Bi-functionality of mesostructured $MnCo_2O_4$ microspheres for supercapacitor and methanol electro-oxidation, *Ceram. Int.*, 2017, **43**, 2670–2679.

5 N. To Van, S. Le The, T. Vu Van, T. Vu Dinh, M. Hatsukano, K. Higashimine, S. Maenosono, S. E. Chun and T. Tran Viet, Facile synthesis of Mn-doped $NiCo_2O_4$ nanoparticles with enhanced electrochemical performance for a battery-type supercapacitor electrode, *Dalton Trans.*, 2020, **49**, 6718–6729.

6 Y. Guo, L. Yu, C. Y. Wang, Z. Lin and X. W. D. Lou, Hierarchical tubular structures composed of Mn-based mixed metal oxide nanoflakes with enhanced electrochemical properties, *Adv. Funct. Mater.*, 2015, **25**, 5184–5189.

7 C. Zhong, Y. Deng, W. Hu, J. Qiao, L. Zhang and J. Zhang, A review of electrolyte materials and compositions for electrochemical supercapacitors, *Chem. Soc. Rev.*, 2015, **44**, 7484–7539.

8 Y. Gogotsi and R. M. Penner, Energy storage in nanomaterials-capacitive, pseudocapacitive, or battery-like?, *ACS Nano*, 2018, **12**, 2081–2083.

9 T. Brousse, D. Belanger and J. W. Long, To be or not to be pseudocapacitive?, *J. Electrochem. Soc.*, 2015, **162**, A5185–A5189.

10 A. C. Forse, C. Merlet, J. M. Griffin and C. P. Grey, New perspectives on the charging mechanisms of supercapacitors, *J. Am. Chem. Soc.*, 2016, **138**, 5731–5744.

11 F. Ran, X. Yang and L. Shao, Recent progress in carbon-based nanoarchitectures for advanced supercapacitors, *Adv. Compos. Hybrid Mater.*, 2018, **1**, 32–55.

12 S. Najib and E. Erdem, Current progress achieved in novel materials for supercapacitor electrodes: mini review, *Nanoscale Adv.*, 2019, **1**, 2817–2827.

13 V. Augustyn, P. Simon and B. Dunn, Pseudocapacitive oxide materials for high-rate electrochemical energy storage, *Energy Environ. Sci.*, 2014, **7**, 1597–1614.

14 F. Liao, X. Han, D. Cheng, Y. Zhang, X. Han, C. Xu and H. Chen, MnO_2 hierarchical microspheres assembled from porous nanoplates for high-performance supercapacitors, *Ceram. Int.*, 2019, **45**, 1058–1066.

15 J. Sun, X. Du, R. Wu, Y. Zhang, C. Xu and H. Chen, Bundlelike $CuCo_2O_4$ microstructures assembled with ultrathin nanosheets as battery-type electrode materials for high-performance hybrid supercapacitors, *ACS Appl. Energy Mater.*, 2020, **3**, 8026–8037.

16 Y. Shao, M. F. El-Kady, J. Sun, Y. Li, Q. Zhang, M. Zhu, H. Wang, B. Dunn and R. B. Kaner, Design and mechanisms of asymmetric supercapacitors, *Chem. Rev.*, 2018, **118**, 9233–9280.

17 Y. Wang, S. Li, J. Sun, Y. Zhang, H. Chen and C. Xu, Simple solvothermal synthesis of magnesium cobaltite microflowers as a battery grade material with high electrochemical performances, *Ceram. Int.*, 2019, **45**, 14642–14651.

18 W. Jiang, F. Hu, Q. Yan and X. Wu, Investigation on electrochemical behaviors of $NiCo_2O_4$ battery-type supercapacitor electrodes: the role of an aqueous electrolyte, *Inorg. Chem. Front.*, 2017, **4**, 1642–1648.

19 J. Sun, S. Li, X. Han, F. Liao, Y. Zhang, L. Gao, H. Chen and C. Xu, Rapid hydrothermal synthesis of snowflake-like $ZnCo_2O_4$/ZnO mesoporous microstructures with excellent electrochemical performances, *Ceram. Int.*, 2019, **45**, 12243–12250.

20 X. Li, M. Zhang, L. Wu, Q. Fu and H. Gao, Annealing temperature dependent $ZnCo_2O_4$ nanosheet arrays supported on Ni foam for high-performance asymmetric supercapacitor, *J. Alloys Compd.*, 2019, **773**, 367–375.

21 J. Sun, X. Du, R. Wu, H. Mao, C. Xu and H. Chen, Simple synthesis of honeysuckle-like $CuCo_2O_4$/CuO composites as a battery type electrode material for high-performance hybrid supercapacitors, *Int. J. Hydrogen Energy*, 2021, **46**, 66–79.

22 H. Chen, X. Du, J. Sun, Y. Wang, Y. Zhang and C. Xu, Solvothermal synthesis of novel pod-like $MnCo_2O_{4.5}$ microstructures as high-performance electrode materials for supercapacitors, *Int. J. Hydrogen Energy*, 2020, **45**, 3016–3027.

23 C. Liu, Y. Xia, Y. Zhang, Q. Y. Zhou, H. B. He, F. D. Yu, Z. R. Wu, J. Liu, X. L. Sui, M. Gu and Z. B. Wang, Pseudocapacitive crystalline $MnCo_2O_{4.5}$ and amorphous $MnCo_2S_4$ core/shell heterostructure with graphene for high-performance K-ion hybrid capacitors, *ACS Appl. Mater. Interfaces*, 2020, **12**, 54773–54781.

24 W. Li, K. Xu, G. Song, X. Zhou, R. Zou, J. Yang, Z. Chen and J. Hu, Facile synthesis of porous $MnCo_2O_{4.5}$ hierarchical architectures for high-rate supercapacitors, *CrystEngComm*, 2014, **16**, 2335–2339.

25 F. Liao, X. Han, Y. Zhang, C. Xu and H. Chen, Solvothermal synthesis of porous $MnCo_2O_{4.5}$ spindle-like microstructures as high-performance electrode materials for supercapacitors, *Ceram. Int.*, 2018, **44**, 22622–22631.

26 K. Wang, J. Xu, A. Lu, Y. Shi and Z. Lin, Coordination polymer template synthesis of hierarchical $MnCo_2O_{4.5}$ and $MnNi_6O_8$ nanoparticles for electrochemical capacitors electrode, *Solid State Sci.*, 2016, **58**, 70–79.

27 L. Kuang, F. Ji, X. Pan, D. Wang, X. Chen, D. Jiang, Y. Zhang and B. Ding, Mesoporous $MnCo_2O_{4.5}$ nanoneedle arrays electrode for high-performance asymmetric supercapacitor application, *Chem. Eng. J.*, 2017, **315**, 491–499.

28 A. Pendashteh, J. Palma, M. Anderson and R. Marcilla, Facile synthesis of $NiCoMnO_4$ nanoparticles as novel electrode materials for high-performance asymmetric energy storage devices, *RSC Adv.*, 2016, **6**, 28970–28980.

29 H. Chen, X. Du, J. Sun, R. Wu, Y. Wang and C. Xu, Template-free synthesis of novel Co_3O_4 micro-bundles assembled with flakes for high-performance hybrid supercapacitors, *Ceram. Int.*, 2021, **47**, 716–724.

30 R. Yuan, H. Li, X. A. Zhang, H. Zhu, J. Zhao and R. Chen, Facile one-pot solvothermal synthesis of bifunctional chrysanthemum-like cobalt-manganese oxides for supercapacitor and degradation of pollutants, *J. Energy Storage*, 2020, 29.

31 M. Zhang, W. Liu, R. Liang, R. Tjandra and A. Yu, Graphene quantum dot induced tunable growth of nanostructured $MnCo_2O_{4.5}$ composites for high-performance supercapacitors, *Sustainable Energy Fuels*, 2019, **3**, 2499–2508.

32 H. Chen, J. Wang, F. Liao, X. Han, C. Xu and Y. Zhang, Facile synthesis of porous Mn-doped Co_3O_4 oblique prisms as an electrode material with remarkable pseudocapacitance, *Ceram. Int.*, 2019, **45**, 8008–8016.

33 H. Che, Y. Lv, A. Liu, H. Li, Z. Guo, J. Mu, Y. Wang and X. Zhang, $MnCo_2O_4$@$Co(OH)_2$ coupled with N-doped carbon nanotubes@reduced graphene oxide nanosheets as electrodes for solid-state asymmetric supercapacitors, *Chem. Eng. J.*, 2020, 384.

34 P. Hao, Z. Zhao, L. Li, C. C. Tuan, H. Li, Y. Sang, H. Jiang, C. P. Wong and H. Liu, The hybrid nanostructure of $MnCo_2O_{4.5}$ nanoneedle/carbon aerogel for symmetric supercapacitors with high energy density, *Nanoscale*, 2015, **7**, 14401–14412.

35 M. Haripriya, A. M. Ashok, S. Hussain and R. Sivasubramanian, Nanostructured $MnCo_2O_4$ as a high-performance electrode for supercapacitor application, *Ionics*, 2020, **1**, 325–337.

36 Z. Wang, F. Wei, Y. Sui, J. Qi, Y. He and Q. Meng, A novel core-shell polyhedron Co_3O_4/$MnCo_2O_{4.5}$ as electrode materials for supercapacitors, *Ceram. Int.*, 2019, **45**, 12558–12562.

37 H. Mu, X. Su, Z. Zhao, C. Han, Z. Wang and P. Zhao, Facile synthesis of $Ni_{0.5}Mn_{0.5}Co_2O_4$ nanoflowers as high-performance electrode material for supercapacitors, *J. Am. Ceram. Soc.*, 2019, **102**, 6893–6903.

38 B. Saravanakumar, X. Wang, W. Zhang, L. Xing and W. Li, Holey two dimensional manganese cobalt oxide nanosheets as a high-performance electrode for supercapattery, *Chem. Eng. J.*, 2019, **373**, 547–555.

39 Y. Gao, Y. Xia, H. Wan, X. Xu and S. Jiang, Enhanced cycle performance of hierarchical porous sphere $MnCo_2O_4$ for asymmetric supercapacitors, *Electrochim. Acta*, 2019, **301**, 294–303.

40 F. Li, G. Li, H. Chen, J. Q. Jia, F. Dong, Y. B. Hu, Z. G. Shang and Y. X. Zhang, Morphology and crystallinity-controlled synthesis of manganese cobalt oxide/manganese dioxides hierarchical nanostructures for high-performance supercapacitors, *J. Power Sources*, 2015, **296**, 86–91.